Article

Development of catalytic zero-valent iron incorporated PAN catalytic film for efficient degradation of organic matters

Check for updates

Yi Yang[1,2] ✉, Haowen Lin[1], Yuxi Long[1], Ying Mei[3] & J. Paul Chen [iD] [4,5] ✉

Catalytic films work well in degradation of organic matters. However, catalytic activity and stability of films are challenging factors. A nanoscale zero-valent iron (NZVI) incorporated porous PAN fiber (Fe-PAN) film was thus developed through a one-step cryogenic auxiliary electrospinning method. The Fe-PAN film overcame the problem in the traditional multistep preparation process. The excellent intrinsic properties of the polymer in the film were maintained. It exhibited high catalytic activity (> 95% conversion in just 4 min) and excellent stability and reusability, due to the synergistic interaction between PAN and NZVI. The degradation process was optimized by the Box-Behnken design, leading to the optimal condition: pH = 2.8, temperature = 56 °C, and oxidant concentration = 4.2 mmol/L. The degradation followed the 2nd order kinetic equation and was due to the reactions by $\cdot OH$ and O_2^- radicals. This study demonstrates the great potentials of the Fe-PAN film for industrial applications.

Organic contamination has caused various environmental problems. Traditionally, it is treated by activated sludge process; however, it does not work well when the organic concentrations are at the lower levels (e.g., <50 mg/L Chemical Oxygen Demand (COD)). As such, adsorption, advanced oxidation process (AOP), membrane filtration, and ion exchange are commonly used for solving the problem. The heterogeneous catalytic wet peroxide oxidation (CWPO) technology has attracted great attentions due to its simplicity in operation and low operational cost[1,2].

Among several heterogeneous catalysts, nanoscale zero-valent iron (NZVI) has shown its advantages: low cost, environmental-friendliness and high efficiency[3,4]. However, the technology has a few problems: easy oxidation on surfaces and difficulty in separation. Decrease in catalytic efficiency, loss of NZVI and secondary pollution are commonly reported[5].

One of the most effective solutions is to load NZVI onto stable porous substrate(s). Polymeric fiber films are suitable due to strong resistance to corrosion, excellent mechanical strength, ease in modification, good ductility and high voidage[6,7]. The abundant π electrons in polymer(s) lead to strong electrostatic effects to bind iron nanoparticles with the conjugated structures. The synergistic interaction between the nanoparticles and the fibers would lead to the enhancement in both catalytic activity and stability than inorganic catalysts[8,9].

Electrospinning is an innovative technology to fabricate polymer fiber films that can perform well in separation and reactions[10–12]. The structural characteristics (e.g., diameter, pore size, porosity and thickness) can be better controlled and achieved by adjusting the operational parameters (e.g., voltage). However, the traditional methods to combine metal based materials and films often have multistep, such as hydrothermal processes, redox reactions, calcination and surface modification. These steps make the preparation process time-consuming and costly[13]. Additionally, such approaches may lead to uneven distribution of active component(s), decrease in catalytic efficiency, low mechanical strength and damage to polymer structure[8]. The interactions between the nanoparticles and the fibers are generally weak, causing nanoparticle leakage, fast deactivation and hence secondary contamination[14].

Catalytic activity and stability of catalytic film are two key factors in performance in the operations[15]. High stability is always accompanied by low activity. In this study, we developed an innovative electrospinning approach to fabricate a stable and efficient water treatment material combined with NZVI and fiber (film). The thermally induced phase separation (TIPS) method was used to fabricate material that is anticipated to have high stability and porosity. The polymers with different solubilities interacted with the solvent(s) at different temperatures. A high freezing rate can therefore be achieved and the low freezing temperature can lead to formation of fibers

[1]Faculty of Arts and Sciences/College of Education for the Future, Beijing Normal University, Zhuhai 519087, P.R. China. [2]Guangdong Provincial Key Laboratory of Wastewater Information Analysis and Early Warning, Beijing Normal University, Zhuhai 519087, P.R. China. [3]Research and Development Center for Watershed Environmental Eco-Engineering, Beijing Normal University, Zhuhai 519087, P.R. China. [4]Department of Civil and Environmental Engineering, National University of Singapore, Kent Ridge Crescent, Singapore 119260, Singapore. [5]College of Chemistry and Environmental Engineering, Shenzhen University, Shenzhen, China. ✉e-mail: yiyang@bnu.edu.cn; jpaulchen@u.nus.edu

with more porous fibrous structures[16]. Briefly speaking, the NZVI was entrapped inside of porous PAN fiber prepared through a one-step electrospinning technique assisted by liquid nitrogen. Therefore, a highly porous NZVI incorporated PAN fiber film (Fe-PAN) can be produced.

The main objectives of this study were: (1) to synthesize and characterize the novel Fe-PAN catalyst; (2) to optimize reaction conditions of the CWPO over Fe-PAN, in which methylene blue (MB) was chosen as a model organic compound due to its higher toxicity and wide applications[17–19]; and (3) to investigate reaction mechanism(s) and confirm the roles of reactive oxygen species (ROS) on the degradation as well as monitor the catalyst structural evolution.

Results and discussions
Structural characterization

An inverse relationship typically exists between catalytic activity and stability for traditional catalytic films[15]. For the nano-metals loaded films, a higher contact efficiency between the surface-active component can initially be achieved. However, agglomeration may occur and reduce the utilization efficiency of nano-metals. Additionally, the weak interaction between the nanometals and the polymer fiber leads to severe detachment of nanomaterials and metal leakage, causing rapid catalyst deactivation and the risk of secondary pollution.

For the films with entrapment of nano-metals, coordination and complexation between nano-metals and polymers improve the stability of composites. However, the contact efficiency and mass transfer between reactants and the entrapped nano-metals are affected. This problem can be solved by the unique structure of Fe-PAN as shown in Fig. 1, in which the entrapped NZVI and porous PAN fiber were combined to ensure the catalyst stability and contact efficiency simultaneously.

The advanced 3D network structure of Fe-PAN was shown in Fig. 1b, which played a key role in decreasing external diffusion resistance of pollutant[20]. The surface and internal structures of the Fe-PAN and C-Fe-PAN were shown in the figures. In Fig. 1d, e, the formation of porous structures can be seen on the surface and in the interior of the Fe-PAN fibers. These unique porous structures effective reduced the internal diffusion resistance during reactions and allowed the reactants to easily penetrate the fibers. Figure 1f suggested that the NZVI particles were successfully incorporated inside the fibers. As a result, the reaction efficiency between the reactants and NZVI was strongly improved by simultaneous strengthening of both internal and external diffusion of the reactants. For C-Fe-PAN, the cross section shows that the fiber was solid inside, and the fibrous surface was smooth and continuous as shown in Fig. 1g, h. In this way, the pollutants cannot sufficiently connect with the NZVI inside, thus affecting the reaction efficiency.
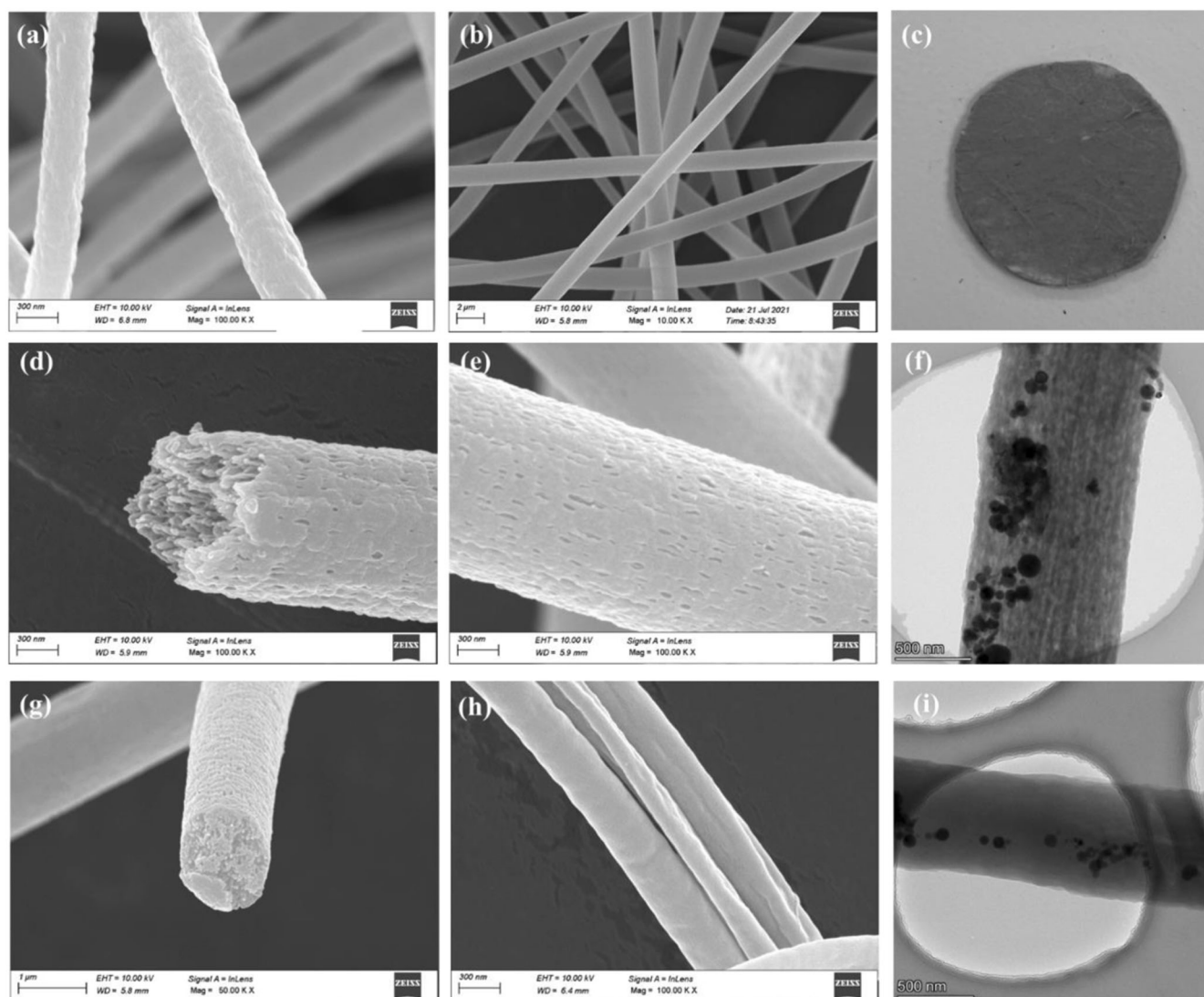
Fig. 1 | Structure of Fe-PAN samples. a Texture of pure PAN fiber, (**b**) three-dimensional structure of Fe-PAN, (**c**) photograph of Fe-PAN, (**d**) and (**e**) texture of Fe-PAN, (**f**) inner structure of Fe-PAN, (**g**) and (**h**) texture of C-Fe-PAN and (**i**) inner structure of C-Fe-PAN.
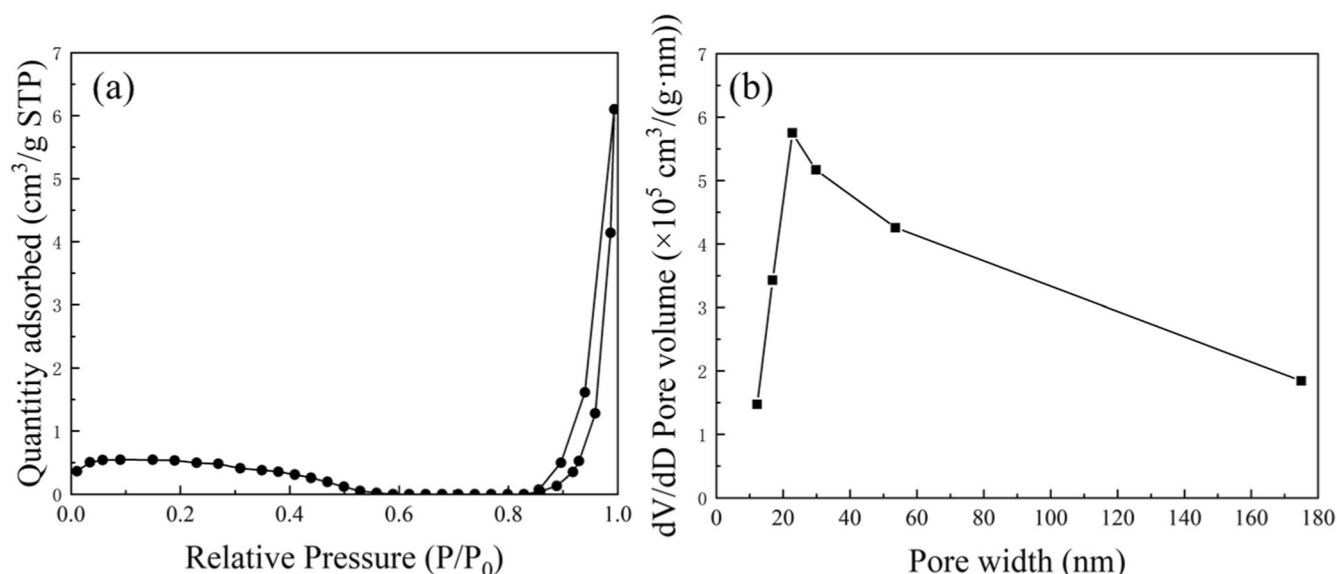
Fig. 2 | Study of physical properties of Fe-PAN. a N_2 adsorption-desorption isotherm; (b) pore width.

During the cryogenic auxiliary electrospinning, the rapid evaporation of solvent led to the solidification of fiber, and the remaining solvent became frozen with the polymer as soon as the precursor reached the collector, and the TIPS process occurred[21]. A large temperature gradient significantly improved the driving force in the phase separation. Simultaneously, phase separation into solvent-rich and solvent-poor regions was induced[22]. The polymer-rich regions vitrified due to the low temperature below its glass transition temperature. As a result, the solvent evaporation rate became different, and the porous structure was obtained after drying[23]. During the electrospinning process, NZVI was simultaneously incorporated into the PAN fiber, and the porous Fe-PAN fiber could be synthesized in one step.

The SEM results showed that the diameter of the Fe-PAN was approximately 500-1000 nm, which was larger than that of the pure PAN fiber (200-300 nm). The entrapped NZVI led to an increase in the fiber diameter[24]. According to previous research, an increase in the fiber diameter would lead to an increase in the average pore size[25]. However, the average pore size of Fe-PAN was much smaller than that of the modified PAN fiber, indicating that cryogenic auxiliary electrospinning was helpful for developing fibers with abundant nano-mesopores.

The TEM images (Fig. 1f, i) and EDS mapping (Supplementary Fig. 1) confirmed that NZVI was successfully entrapped inside the PAN fiber. The density was 3.2×10^{10} and 2.2×10^{10} particle/μm^3 for Fe-PAN and C-Fe-PAN, respectively. The density of NZVI in Fe-PAN was 30% larger than that in C-Fe-PAN. The increase in the polymer conductivity under ultracold condition was beneficial for the entrapment of NZVI[26,27]. The shorter distance in Fe-PAN between the NZVI particles increased the local catalyst concentration and the contact efficiency during the reaction, and thus improved the reaction rate. After the reactants penetrated the Fe-PAN fiber, a confining effect occurred[28] to increase the reaction driving force and contact efficiency. A large number of reactive oxygen species (ROS) were generated and fully consumed to react with the pollutants. The catalytic efficiency were thus significantly improved[29], and the destruction effect of ROS towards the polymer fiber was reduced to extend the catalyst service life[30].

Supplementary Fig. 2 showed the AFM images of Fe-PAN. The averaged surface roughness of Fe-PAN was 21.2 nm, which was smaller than the commonly reported modified PAN fiber (about 30–50 nm)[31]. In this study, the one-step porous Fe-PAN synthesis method avoided the surface destruction in traditional multiple-step preparation[32]. As a result, the stability and mechanical strength were significantly improved.

The hierarchical porosity of Fe-PAN was determined by the study on the N_2 adsorption-desorption isotherm with the result given in Fig. 2a. A typical type II standard isotherm is observed, indicating the existence of macropores in the developed three-dimensional network structure[33,34]. Macropores promoted the transfer of reactants from the bulk solution to the catalysts and the release of byproducts on the surface[35,36]. The catalytic efficiency was therefore improved and surface coke formation was avoided. The isotherm showed a hysteresis loop at high P/P_0, making it similar to type IV[37] and indicating the existence of mesopores with a narrow size distribution[38], which enhances the contact efficiency between the internal NZVI and the reactants[39].

The BJH pore size distribution was shown in Fig. 2b. The pore width in Fe-PAN was mainly within 20–50 nm. The BET surface area (S_{BET}) of Fe-PAN (1.48 m^2/g) was slightly higher than the typical electrospun PAN fibers (0.1–1 m^2/g) and similar to that of C-Fe-PAN (1.33 m^2/g). However, its S_{BET} was smaller than that of PAN fibers modified by calcination, hydrothermal treatment or alkali treatment. An increase in diameter of Fe-PAN due to the NZVI coating led to a decrease in the S_{BET}[25]. Unlike the common modified PAN fiber, the evenly dispersed nano-meso pores in Fe-PAN catalytic film help greatly to protect the NZVI from leaching.

As shown in Supplementary Fig. 3, the contact angle of the Fe-PAN film was larger than 90°, indicating poor wettability. However, the PAN fiber was hydrophilic, and the penetration of organic pollutant into the fiber was not affected. The film still showed excellent pollutant degradation ability in the CWPO reaction (to be discussed later). Additionally, hydrophobic films are beneficial for film contactor applications such as membrane distillation. Hence, the Fe-PAN film may achieve catalytic degradation and distillation simultaneously in one process.

Good balance should be sought between catalytic degradation and water flux. The catalytic performance can be improved by increasing the film thickness. However, it would lead to a sharp decrease in water flux, causing lower treatment efficiency and an increase in time and cost. On the other hand, an increase in water flux is usually accompanied by a decrease in catalytic efficiency due to insufficient residence time for organic contaminant(s). As a result, it is necessary to prepare catalytic films with high catalytic efficiency and water flux[40].

The water flux (J_w) of Fe-PAN film was tested with the finding given in Supplementary Fig. 4. The average J_w of Fe-PAN was 1361.5 m^{-2} h^{-1} bar^{-1}, which far exceeded that of reported catalytic films for MB degradation (1.3–123 times higher) as listed in Supplementary Table 1. The high J_w indicated a great water permeation ability of Fe-PAN. Additionally, Fe-PAN also showed higher efficiency in MB degradation (later discussed). The unique three-dimensional network structure of Fe-PAN ensured superior water flux, while better contact efficiency and

synergistic interaction between PAN and NZVI contributed to greater catalytic performance.

Optimization of degradation process

The CWPO reaction process driven by Fe-PAN was optimized by a three-level Box–Behnken design. The effects of selected independent variables of pH (A), temperature (°C) (B) and oxidant (H_2O_2) concentration (C) on the responses (degradation efficiency, expressed by MB removal of C/C_0) were evaluated. This design is suitable for the derivation of second-order polynomial models to depict the effects of different independent factors on the dependent response[41]. The experimental ranges and levels of the independent test variables were given in Supplementary Tables 2, and 17 experiments were conducted (Supplementary Table 3).

The results of analysis of variance (ANOVA) were shown in Supplementary Table 4 so as to verify the significance and adequacy of the model. A high determination coefficient (r^2) value of 0.99 indicated a good correlation between the experimental and predicted values of the fitted data in the model, as shown in Supplementary Fig. 5. The predicted r^2 value of 0.82 was in reasonable agreement with the adjusted r^2 value of 0.97, as the difference was less than 0.2. The Adeq Precision was 26.409 (far above 4), suggesting the great suitability of model to navigate the design space. Fisher's F-test was used to verify the statistical significance of model. The Model F-value (ratio of mean square regression to mean square residual) was 67.15 with a p value < 0.0001, implying that the model was significant[42].

The significance of the model terms can be verified by the value of "Prob > F", which indicates a significant model term when it is less than 0.0500[43]. In the design, A (pH), B (Temperature), AB, A^2, and B^2 were significant model terms. The values greater than 0.1000 indicated insignificant model terms, suggesting that oxidant concentration had little effect on MB removal. This result was consistent with previous research on reaction over zero-valent iron (Fe^0)[44].

Through the simulation, the equations in terms of coded and actual factors were obtained and therefore were used to make predictions about the response as shown in Eqs. (1) and (2), respectively. The coded equation is useful for identifying the relative impact of the factors by comparing the factor coefficients. For the actual factors, the levels of each factor should be specified in the original units.

$$\begin{aligned} X = {} & 0.47 + 0.31 \times A - 0.055 \times B - 0.011 \times C - 0.061 \times AB \\ & - 0.030 \times AC - 0.013 \times BC \\ & - 0.14 \times A^2 + 0.076 \times B^2 + 0.039 \times C^2 \end{aligned} \tag{1}$$

$$\begin{aligned} X = {} & -0.47 + 0.36 \times A - 0.016 \times B - 5.56 \times 10^{-3} \times C - 1.16 \times \\ & 10^{-3} \times AB - 2.02 \times 10^{-3} \times AC \\ & - 1.50 \times 10^{-4} \times BC - 0.16 \times A^2 + 2.47 \times 10^{-4} \times B^2 + 1.56 \\ & \times 10^{-3} \times C^2 \end{aligned} \tag{2}$$

Equation (1) shows that the effect of pH (A) was the most significant while that of oxidant concentration (C) was neglected. Supplementary Fig. 6 shows the influence of one factor with the values of the other two variables fixed at the center point. Both pH and temperature showed an effect on the reaction at a low coded level and then stabilized at a high level. The positive surface of the catalyst under low pH was less beneficial for the degradation due to the electrostatic repulsion with cationic dye[45–47]. Even so, the Fe-PAN film still exhibited high reaction efficiency at low pH. Strong acid conditions favored the generation of oxidative radicals from H_2O_2[48,49] and the capture ability of PAN fiber towards them[50]. Additionally, at low pH, the formation of less oxidative iron species, such as oxyhydroxides and $Fe(OH)^{2+}$, was prevented[51,52], and the oxidation ability of ·OH was enhanced[48]. It is worth noting that very smaller Fe leakage was detected during degradation, confirming the stability of Fe-PAN.

With an increase in temperature, the MB residual concentration first decreased and then remained stable. As the temperature was increased, the
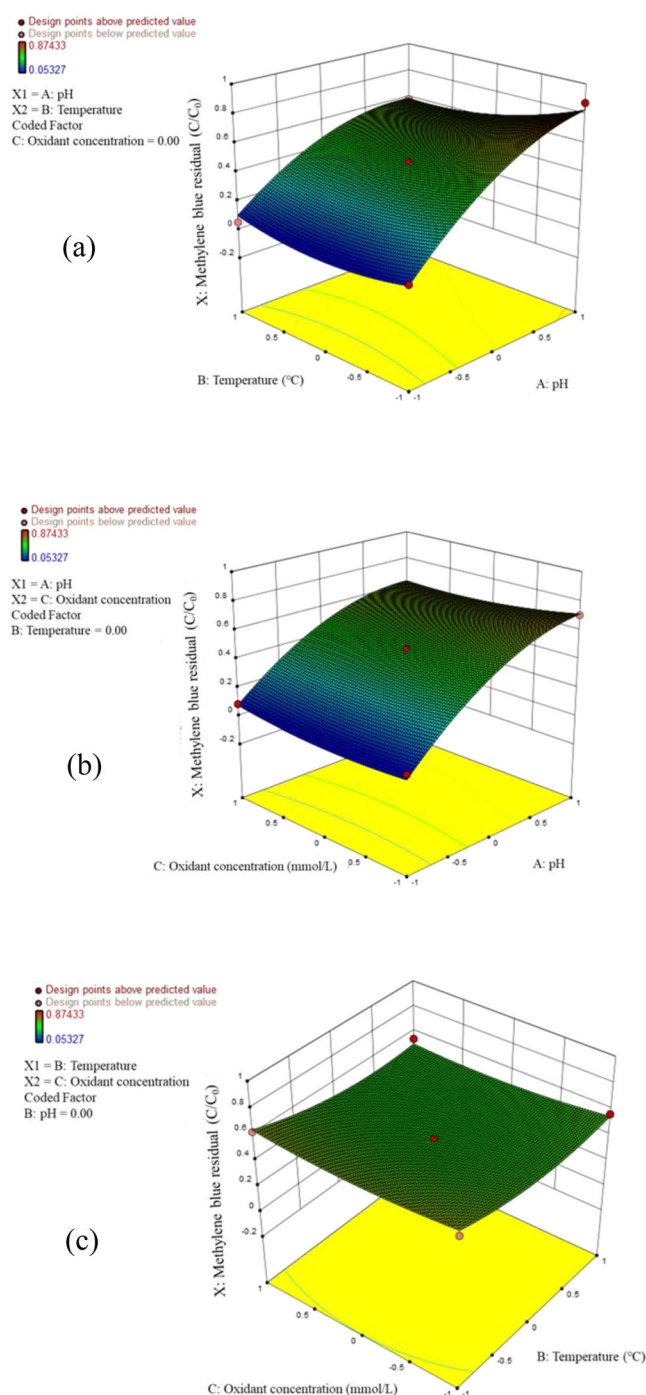
Fig. 3 | 3D surface of interactive effect of different factors. a temperature and pH, (**b**) oxidant concentration and pH and (**c**) temperature and oxidant concentration.

conversion of H_2O_2 into oxidative radicals played a dominant role due to strong electron donation ability and high electron mobility of Fe-PAN[53]. On the other hand, at a higher temperature, the greater decomposition of H_2O_2 into H_2O and O_2 and the scavenging reactions of ROS strongly affected the MB degradation[54]. These factors determined the overall degradation of MB[55]. A moderate temperature would lead to the better degradation. Additionally, the interaction of pH and temperature (factor AB) is significant and has a negative impact on the response.

Figure 3 depicted the 3D surface plot and Supplementary Fig. 7 showed the 2D contour plot for the combined interaction of different factors on the CWPO process. Figure 3a and Supplementary Fig. 7a showed that the worst efficiency occurred at a high pH and a low temperature. Figure 3b and
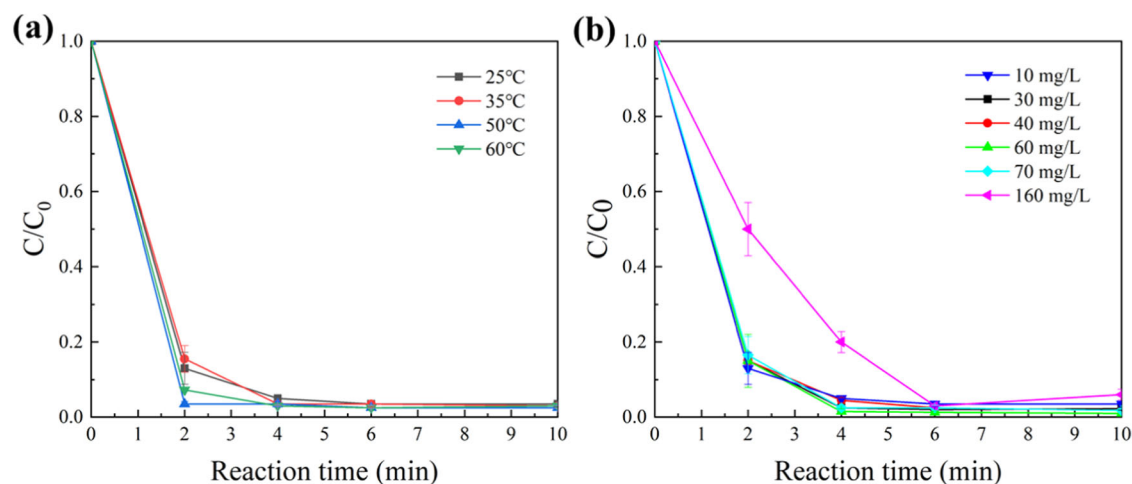
Fig. 4 | CWPO reaction over Fe-PAN. Effects of (**a**) temperature and (**b**) MB concentration.

Supplementary Fig. 7b demonstrated that the effect of pH was more efficient than that of oxidant concentration; the variation of response was just little while the oxidant concentration was changed, especially at low pH. In Fig. 3c and Supplementary Fig. 7c, the contour line of the response was oval, indicating that the reaction efficiency increased first and then decreased for both factors (temperature and oxidant concentration)[56]. The optimum conditions for MB degradation were determined through the simulation: pH = 2.8, temperature = 56°C and oxidant concentration = 4.2 mmol/L; the predicted C/C_0 was 0.04.
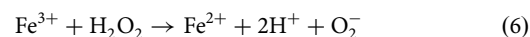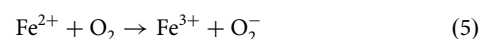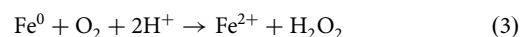
Mechanism analysis

The interference of adsorption on the degradation was excluded by a controlling experiment that was conducted in the absence of H_2O_2; only less than 10% removal was observed. Additionally, the control experiments over the pure PAN and C-Fe-PAN films were conducted, respectively. The results (Supplementary Fig. 8) showed that the pure PAN film had no obvious MB removal (<10%), and the C-Fe-PAN film took over 20 min to reach the similar degradation efficiency under the same conditions. The findings indicated that the entrapped NZVI played an important role in the degradation; the porous structure of Fe-PAN helped greatly to improve the degradation efficiency, which was in line with the results from the study on the structure characterization of Fe-PAN.

Additionally, the catalytic degradation of methyl orange and methyl blue were studied. The results showed that both methyl orange and methyl blue could effectively be degraded (above 90%, data not shown), suggesting the ideal degradation ability of the film. Due to the representativeness of MB as an environmental pollutant with high stability and refractory, it was chosen as a model compound to further analysis the mechanism of the CWPO reaction(s).

As shown in Fig. 4a, the highest degradation efficiency (90%) was observed at 50 °C at the end of 2-min contact. This is consistent with the findings from the optimization study, which demonstrated that a moderate temperature was the most beneficial for the degradation. As discussed above, the increase in temperature led to the acceleration of H_2O_2 degradation into both active radicals and H_2O/O_2. Such inverse influence would significantly affect the degradation[55]. Due to the unique functionality of the Fe-PAN, the degradation could reach over 90% in 4 min under all temperatures. Supplementary Table 5 shows that the Fe-PAN greatly outperforms many reported CWPO catalysts as the Fe-PAN only took 20–30 min to reach the degradation.
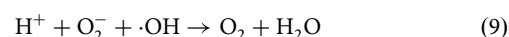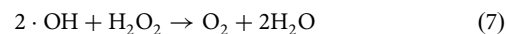
At the concentrations ranging from 10 to 70 mg/L, C/C_0 decreased to less than 0.2 in 2 min and to less than 0.1 in 4 min as shown in Fig. 4b. Typically, the degradation efficiency becomes lower with an increase in reactant concentration due to the constraint of reaction rate. However, the degradation efficiency in this study was not affected by the increased

reactant concentration due to the generation of radicals according to Eqs. (3)–(6) as well as favorable mass transfer property.

$$Fe^0 + O_2 + 2H^+ \rightarrow Fe^{2+} + H_2O_2 \tag{3}$$

$$Fe^{2+} + H_2O_2 \rightarrow \cdot OH + OH^- + Fe^{3+} \tag{4}$$

$$Fe^{2+} + O_2 \rightarrow Fe^{3+} + O_2^- \tag{5}$$

$$Fe^{3+} + H_2O_2 \rightarrow Fe^{2+} + 2H^+ + O_2^- \tag{6}$$

The degradation was greatly controlled by the radicals; the diffusion resistance was minimized by the hierarchical nano-mesoporous structure and the advanced network structure of the Fe-PAN film. From the TEM results, the entrapped NZVI dispersed evenly inside the Fe-PAN and provided sufficient active sites. The confining effect provided a high contact efficiency between the reactants and the NZVI. At the same time, the frost crack of the NZVI surface oxide layer that was caused by the cryogenic process led to a higher electron transfer efficiency between the NZVI and the reactants.

At low contaminant concentrations, the scavenging reactions occurred according to Eqs. (7)–(9), which led to lower radical utilization. When the initial concentration was increased, the utilization of radicals increased and a high degradation efficiency was maintained.

$$2 \cdot OH + H_2O_2 \rightarrow O_2 + 2H_2O \tag{7}$$

$$2 \cdot OH \rightarrow H_2O_2 \tag{8}$$

$$H^+ + O_2^- + \cdot OH \rightarrow O_2 + H_2O \tag{9}$$

However, when the MB concentration was increased to 160 mg/L, C/C_0 decreased to 0.5 in 2 min, and 90% degradation was achieved in 6 min. A high MB concentration might have covered the active sites and resulted in less radical generation[57,58], leading to a lower degradation rate.

The CWPO of MB over Fe-PAN fitted the 2nd reaction kinetics equations better ($r^2 = 0.98$) than the 1st reaction kinetics equation, although in previous reports the reaction should obey the 1st reaction[44,59]. This finding indicated that the Fe-PAN changed the degradation kinetics compared to the traditional catalysts. The confining effect led to more effective collision between the reactants[34], making the process to follow the 2nd order reaction kinetics, in which the availability of the active sites was the controlling factor.

The ROS with key components as $\cdot OH$ and $O_2\cdot$ play an important role in the CWPO[59,60]. To verify their involvement in the degradation, isopropyl

Table 1 | Effects of scavengers on CWPO of MB

Scavenger	k_1 (min^{-1})	r_1^2	k_2 (mg^{-1}·L·min^{-1})	r_2^2	Degradation efficiency (%)
Non	0.54	0.89	0.44	0.98	99
IPA	0.024	0.96	0.0032	0.96	47
p-BQ	0.0036	0.97	0.00040	0.98	17

alcohol (IPA) and p-benzoquinone (p-BQ) were selected for trapping the ·OH and O_2^- species, respectively ($k_{2,p-BQ/O_2^-\cdot} = (0.9-1.0) \times 10^9\,M^{-1}\cdot s^{-1}$, $k_{2,IPA/\cdot OH} = 2.3 \times 10^9\,M^{-1}\cdot s^{-1}$)[61,62]. As shown in Table 1, the presence of IPA (scavenger for ·OH) caused the MB degradation to decrease from 99 to 47%. The addition of p-BQ (scavenger for $O_2^-\cdot$) further decreased the degradation to 17%. The kinetic constants of both 1st (k_1) and 2nd (k_2) equations also decreased significantly and followed the descending sequence of Non scavenger > IPA > p-BQ.

The generation of ·OH and $O_2^-\cdot$ in the CWPO over Fe-PAN was through: (1) the cycle of Fe(II)/Fe(III) as illustrated in Eqs. (3) to (6); and (2) the radical chain transfer process of peroxide shown in Eq. (10)[59,63]. Although the scavengers significantly influenced the MB degradation, they did not fully consume ·OH and $O_2^-\cdot$ likely due to two reasons: (1) the ROS generated through liquid-solid reactions were partially adhered to the Fe-PAN surface and can hardly be totally cleaned up by the scavengers; (2) the confining effect made the ROS not well available in the solution. The ROS reacted with the MB right after their generation from the Fe-PAN fibers. The findings demonstrated that both ·OH and $O_2^-\cdot$ were effective for the degradation of MB, and furthermore the role of $O_2^-\cdot$ was more dominant. The degradation is essentially the Fenton-like reaction, similar to other systems reported[28].

$$\cdot OH + H_2O_2 \rightarrow O_2^- \cdot + H_2O + H^+ \qquad (10)$$
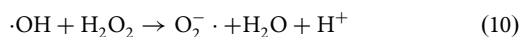
To obtain deeper insight into the degradation mechanism, several cycling runs of Fe-PAN were conducted. The solution after the CWPO was collected and tested by HPLC in order to study the mineralization of MB. No much by-product was detected after the CWPO, suggesting an achievement of the excellent removal of MB through mineralization and/or adsorption. The results given in Supplementary Table 6 showed that the MB could totally be degraded in each cycling run, but the time needed increased significantly from 3 to 75 min. The total iron loss was less than 2 mg/L (1.9% of the total iron loaded), and even after a long-term degradation, the dissolved iron concentration was only 2.75 mg/L (2.6% of the total iron loaded), indicating that the iron leakage was not the cause of the lower efficiency.

The structural change of the Fe-PAN was therefore studied so as to find out the relationship between catalyst structure and degradation performance. Supplementary Fig. 9 showed the surface texture of the Fe-PAN fiber before each cycling run (R1 to R5 corresponding to the 1st to the 5th run, respectively). As the number of runs for reuse increased, the amount of deposited product on the surface of fiber increased, which was ascribed to the deposition of the MB. Although the MB was almost completely removed from the solution, some incompletely degraded by-product (and even MB that was not degraded) might have been adsorbed and attached on the catalyst[64]. As a result, the nano-mesopores on the Fe-PAN fiber became gradually blocked. The blockage decreased the contact efficiency between active NZVI and MB. The Fe-PAN became rougher as the number of reuse runs increased. Such would lower the mechanical strength of the catalytic film and shorten the service life. In Supplementary Fig. 9e, the byproducts even agglomerated and became a kind of "hard coke"[65] attached to the Fe-PAN fiber, further reducing the degradation efficiency.

In the XRD spectra given in Fig. 5a, the characteristic peak of the 110 crystal face of Fe (06-0696, $2\theta = 44.5°$) was shown. No obvious change was observed after the reuse, proving its stability during the degradation. The peak around $2\theta \approx 20°$, which was ascribed to the PAN, showed a shift in the

diffraction angle and exhibited changes in shape due to the decomposition of the organic matter (as shown in Supplementary Fig. 9) and the structural change during the degradation.

To identify the structural change in Fe-PAN, FT-IR and XPS were further conducted. In FT-IR spectra shown in Fig. 5b, the characteristic peaks of PAN could be observed in Fe-PAN samples for every cycling run. A new peak at approximately 800 cm^{-1} appeared after the first run and gradually became stronger. This peak corresponded to the Fe-O stretching vibration[66], indicating the formation of an oxide layer on the active NZVI. As the number of cycling times was increased, the oxide layer became thicker and increased the resistance of electron transport between the NZVI and the reactants. As a result, the oxide layer formation counteracted the benefits of the NZVI frost crack effect and affected the catalytic activity[52].

The wide-scan XPS study with the results given in Supplementary Fig. 10 demonstrates that the peak intensity of O_{1s} increased as the number of cycling was increased, while the intensity of N_{1s} decreased significantly. Supplementary Table 7 showed that the atomic concentration ratio of C_{1s}/O_{1s} decreased (from 15.0 to 5.1) with cycling time. It can be ascribed to the fabrication of hydroxyl groups on the Fe-PAN fiber during the degradation, which was illustrated in the high-resolution spectra of C_{1s} give in Fig. 5c. Three fitting peaks were observed for the Fe-PAN before the 1st and 2nd run, which were ascribed to C-H and C-C (284.8 eV)[67], C-Fe (285.2 eV)[68] and $C \equiv N$ (286.0 eV)[68], respectively. After the 2nd run, a peak corresponding to C-O (288.2 eV)[33,69] appeared. The peak corresponding to $C \equiv N$ decreased significantly with cycling times, and all the peaks moved to a lower binding energy.

Figure 5d showed the high-resolution spectra of O_{1s}. Each spectrum was fitted into two peaks, corresponding to the surface-adsorbed H_2O (533.3 eV) and the fabricated hydroxyl group (531.8 eV), respectively[70]. Similar to the C_{1s} spectra, the peaks in the O_{1s} spectra also moved to a lower binding energy. From the XPS results, it can be derived that the $C \equiv N$ groups in Fe-PAN were replaced by oxygen-containing groups (such as hydroxyl groups). The $C \equiv N$ groups in the PAN structure provided rich π electrons and showed a strong electronic effect with NZVI. These π electrons showed ligand-metal charge transfer (LMCT) effect with the NZVI and strengthened the electron transfer ability during reaction[53]. This effect enabled the electrons on the catalysts to transfer to the reactants faster and more efficiently, thus improving the catalytic reaction efficiency[71].

After the $C \equiv N$ groups were replaced, LMCT effect was weakened and the NZVI became passivated gradually[9]. The decrease in the catalytic activity can therefore be ascribed to three mechanisms: the block of the nano-meso pore, the oxidization of the NZVI and the film structure change (decrease of the $C \equiv N$ groups). Although the structure of the Fe-PAN film changed, it still showed ideal degradation ability compared to reported catalytic films as shown in Supplementary Table 1. As a result, it can be concluded in terms of catalytic ability that, the film showed excellent stability and reusability.

Methods
Fe-PAN preparation
The reagents and materials used in this study are listed in Supplementary Text 1. The preparation process of Fe-PAN catalytic film is demonstrated in Fig. 6a and summarized as follows. 100-g/L PAN and 4-mmol/L TOAB (Tetra-n-octylammonium bromide) were dissolved in DMF; NZVI (Shanghai Macklin Biochemical Co., Ltd, diameter = 50–100 nm, purity = 99.9%) was added to the mixture with the mass ratio of NZVI: PAN = 0.35 and stirred at 200 rpm for 6 h. Ultrasound treatment was then applied for 30 min to evenly disperse the NZVI and obtain the homogeneous suspension.

The porous Fe-PAN fiber was obtained by the cryogenic auxiliary electrospinning that is illustrated in Fig. 6b and was operated under the following conditions: voltage = +10 kV, solution flow rate = 0.1 mm/min and acceptor distance = 4 cm. During the electrospinning, the acceptor was filled with liquid nitrogen. After the electrospinning, the film precursor was freeze-dried for 9 h to obtain Fe-PAN. For comparison, another Fe-PAN film was also prepared by conventional electrospinning (controlled
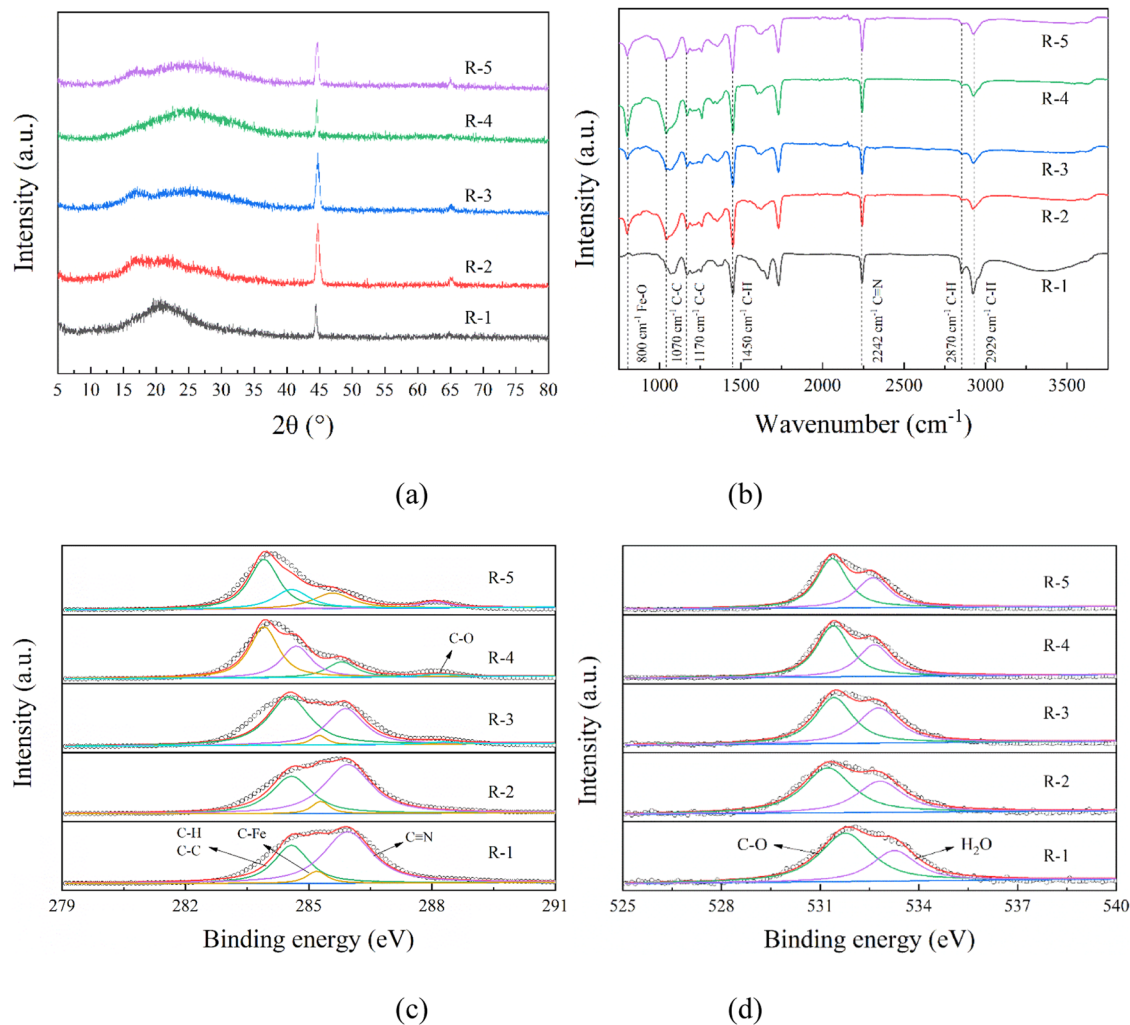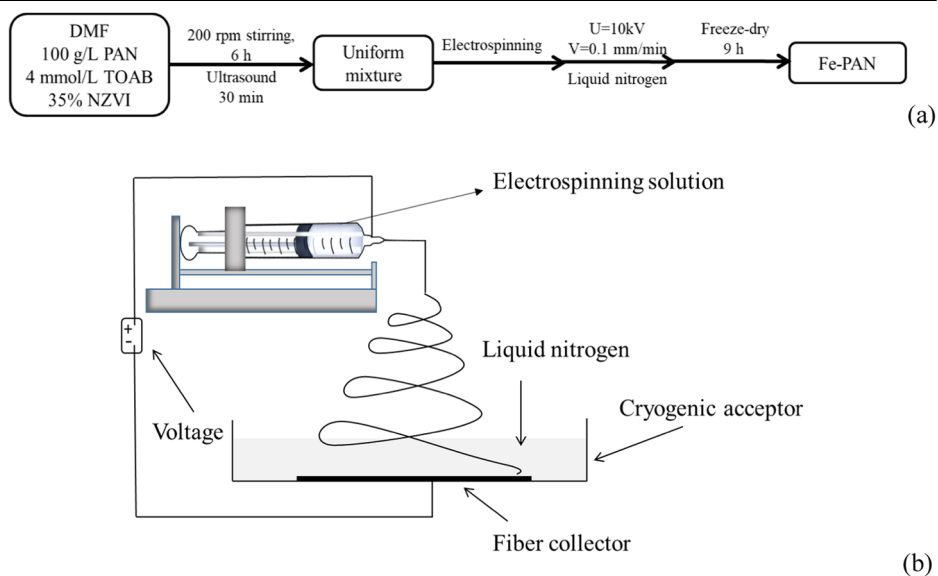
Fig. 5 | Structural change of Fe-PAN sample in each cycling run. a XRD spectra, (**b**) FT-IR spectra, (**c**) XPS C_{1s} spectra and (**d**) XPS O_{1s} spectra.

Fig. 6 | Illustration of Fe-PAN synthesis. a process flowchart; (**b**) schematic diagram of cryogenic auxiliary electrospinning.

Fe-PAN, hereinafter cited as C-Fe-PAN) without cryogenic acceptor and freeze-dry. The characterization methods are described in Supplementary Text 2.

In the conventional electrospinning, fiber becomes evenly solidified immediately after reaching the acceptor. In this study, due to the ultra-cold surrounding provided by the cryogenic acceptor, the electrospinning solution was divided into solvent-rich and solvent-poor regions and was controlled at lower temperature along with the polymer by the TIPS process. Due to the inhomogeneity of the polymer distribution, the porous structure was easily obtained right after drying without furthermore steps.

CWPO over Fe-PAN

The study on CWPO reactions over Fe-PAN was carried out in a batch reactor under atmospheric pressure. The control experiments with C-Fe-PAN as catalyst were also conducted. Typically, 0.4-g/L Fe-PAN was added to 10-mg/L methylene solution (pH = 3) with 2-mmol/L H_2O_2 for 10 min. The detailed experimental processes were described in Supplementary Text 3. The effects of temperature (25–60 °C) and initial MB concentration (10 to 160 mg/L) on CWPO reaction over Fe-PAN were studied. The mineralization of MB was analyzed by the high-performance liquid chromatography (HPLC) on an Agilent 1100 HPLC with a C18 column (100 mm × 2.1 mm, 3 µm). The mobile phase was a mixture of acetonitrile (A) and formic acid solution (1‰) (B) (0-7 min: V_A:V_B = 90:10, 7-9 min: V_A:V_B = 8:92) with the flow rate of 0.3-mL/min and the injection volume of 4-µL. The reaction mechanism was investigated by studying the ROS and the film structural evolution during reaction.

The Box-Behnken design (BBD) study was carried out with three factors to analyze the relationship between the response (C/C_0) and three independent variables (pH, temperature and oxidant concentration). Seventeen runs were conducted to optimize the operational conditions for the degradation of organics. The effects of combined three factors can be expressed by the following second-order polynomial:

$$Y = a_0 + \Sigma a_i X_i + \Sigma a_{ii} X_i^2 + \Sigma a_{ij} X_i X_j \qquad (11)$$

where Y is the predicted response; a_0 is the constant coefficient; a_i and a_{ii} are the linear and quadratic coefficients, respectively; a_{ij} is the interaction coefficient; and X_i and X_j are the coded or actual independent variates.

Furthermore, the catalytic degradation of two different dyes (methyl orange and methyl blue) were studied so as to confirm the degradation performances and better understand the suitability of Fe-PAN for other types of wastewater. The experimental conditions were set as follows: 0.4-g/L Fe-PAN, 10-mg/L pollutant concentration, pH = 3, 2-mmol/L H_2O_2, room temperature, and 10-min reaction time.

Data availability

The data in this paper can be available upon a written official request to the corresponding authors for non-commercial applications.

References

1. Lü, Y. et al. The roles of pyrite for enhancing reductive removal of nitrobenzene by zero-valent iron. *Appl. Catal. B-Environ.* **242**, 9–18 (2019).
2. Yang, Y. et al. A novel bimetallic Fe-Cu-CNT catalyst for effective catalytic wet peroxide oxidation: Reaction optimization and mechanism investigation. *Chem. Eng. J.* **479**, 147320 (2024).
3. Lumbaque, E. C., Tiburtius, E. R. L., Barreto-Rodrigues, M. & Sirtori, C. Current trends in the use of zero-valent iron (Fe0) for degradation of pharmaceuticals present in different water matrices. *Trends Environ. Anal. Chem.* **24**, e69 (2019).
4. Pasinszki, T. & Krebsz, M. Synthesis and application of zero-valent iron nanoparticles in water treatment, environmental remediation, catalysis, and their biological effects. *Nanomaterials* **10**, 917 (2020).
5. Al-Shamsi, M. A. & Thomson, N. R. Treatment of organic compounds by activated persulfate using nanoscale zerovalent iron. *Ind. Eng. Chem. Res.* **52**, 13564–13571 (2013).
6. Si, Y. et al. Superelastic and superhydrophobic nanofiber-assembled cellular aerogels for effective separation of oil/water emulsions. *Acs Nano.* **9**, 3791–3799 (2015).
7. Salunkhe, R. R. et al. Ultrahigh performance supercapacitors utilizing core-shell nanoarchitectures from a metal-organic framework-derived nanoporous carbon and a conducting polymer. *Chem. Sci.* **7**, 5704–5713 (2016).
8. Morselli, D. et al. Ceria/gold nanoparticles in situ synthesized on polymeric membranes with enhanced photocatalytic and radical scavenging activity. *Acs Appl. Nano Mater.* **1**, 5601–5611 (2018).
9. Jin, W. et al. Polyaniline hollow tubes loading tiny platinum nanoparticles for boosting methanol oxidation. *Appl. Surf. Sci.* **483**, 489–495 (2019).
10. Li, K. K. et al. Fabrication of tunable hierarchical MXene@AuNPs nanocomposites constructed by self-reduction reactions with enhanced catalytic performances. *Sci. China Mater.* **61**, 728–736 (2018).
11. Jiang, S. H., Hou, H. Q., Agarwal, S. & Greiner, A. Polyimide nanofibers by "Green" electrospinning via aqueous solution for filtration applications. *Acs Sustain. Chem. Eng.* **4**, 4797–4804 (2016).
12. Yang, Y. et al. Catalytic reaction intensification by a novel cryogenic auxiliary synthesized Fe-PAN membrane. *Ind. Eng. Chem. Res.* **62**, 20677–20688 (2023).
13. Dessbesell, L. et al. Production of 2,5-furandicarboxylic acid (FDCA) from starch, glucose, or high-fructose corn syrup: techno-economic analysis. *Biofuels, Bioprod. Biorefin.* **13**, 1234–1245 (2019).
14. Li, Y., Zhao, H. J. & Yang, M. J. TiO2 nanoparticles supported on PMMA nanofibers for photocatalytic degradation of methyl orange. *J. Colloid Interface Sci.* **508**, 500–507 (2017).
15. Jiang, H. et al. Preparation of carbon nanofibrous mats encapsulating zero-valent Fe nanoparticles as Fe reservoir for removal of organic pollutants. *Rsc Adv.* **11**, 4883–4889 (2021).
16. Nguyen, H. Q. & Deng, B. Electrospinning and in situ nitrogen doping of TiO2/PAN nanofibers with photocatalytic activation in visible lights. *Mater. Lett.* **82**, 102–104 (2012).
17. García, M. C. et al. Microwave atmospheric pressure plasma jets for wastewater treatment: Degradation of methylene blue as a model dye. *Chemosphere* **180**, 239–246 (2017).
18. Zhao, G. Q. et al. Reduced graphene oxide modified NiFe-calcinated layered double hydroxides for enhanced photocatalytic removal of methylene blue. *Appl. Surf. Sci.* **434**, 251–259 (2018).
19. Bavi, A., Jafari, M. S., Heydari, M., Ebrahimi, F. & Sadeghizadeh, A. Batch and continuous mode adsorption of methylene blue cationic dye onto synthesized titanium dioxide/polyurethane nanocomposite modified by sodium dodecyl sulfate. *Colloids Surf. C: Environ. Asp.* **1**, 100012 (2023).
20. Yang, Y. Fixed bed adsorption of phosphate by lanthanum carbonate modified microfibrous composite. *Colloids Surf. C: Environ. Asp.* **1**, 100007 (2023).
21. Kim, J. F., Kim, J. H., Lee, Y. M. & Drioli, E. Thermally induced phase separation and electrospinning methods for emerging membrane applications: A review. *Aiche J.* **62**, 461–490 (2016).
22. Sarazin, P., Roy, X. & Favis, B. D. Controlled preparation and properties of porous poly(l-lactide) obtained from a co-continuous blend of two biodegradable polymers. *Biomaterials* **25**, 5965–5978 (2004).
23. Hyuk Im, S., Jeong, U. & Xia, Y. N. Polymer hollow particles with controllable holes in their surfaces. *Nat. Mater.* **4**, 671–675 (2005).

24. Zheng, S. Y. et al. Integration of a photo-fenton reaction and a membrane filtration using CS/PAN@FeOOH/g-C3N4electrospun nanofibers: Synthesis, characterization, self-cleaning performance and mechanism. *Appl. Catal. B-Environ.* **281**, 119519 (2021).

25. Ryu, Y. J., Kim, H. Y., Lee, K. H., Park, H. C. & Lee, D. R. Transport properties of electrospun nylon 6 nonwoven mats. *Eur. Polym. J.* **39**, 1883–1889 (2003).

26. Chen, X. B., Issi, J. P., Ca Ssart, M., Devaux, J. & Billaud, D. Temperature dependence of the conductivity in conducting polymer composites. *Polymer* **35**, 5256–5258 (1994).

27. Tarhini, A., Alchamaa, M. W., Khraiche, M., Kazan, M. & Tehrani-Bagha, A. The effect of temperature on the electrical and thermal conductivity of graphene-based polymer composite films. *J. Appl. Polym. Sci.* **139**, 51896 (2022).

28. Chen, Y., Zhang, G., Liu, H. J. & Qu, J. H. Confining free radicals in close vicinity to contaminants enables ultrafast fenton-like processes in the interspacing of MoS2 membranes. *Angew. Chem. Int. Ed.* **58**, 8134–8138 (2019).

29. Leus, K. et al. Catalytic carpets: Pt@MIL-101@electrospun PCL, a surprisingly active and robust hydrogenation catalyst. *J. Catal.* **360**, 81–88 (2018).

30. Yu, L., Ling, R., Chen, J. P. & Reinhard, M. Quantitative assessment of the iron-catalyzed degradation of a polyamide nanofiltration membrane by hydrogen peroxide. *J. Membr. Sci.* **588**, 117154 (2019).

31. Almasian, A., Mahmoodi, N. M. & Olya, M. E. Tectomer grafted nanofiber: Synthesis, characterization and dye removal ability from multicomponent system. *J. Ind. Eng. Chem.* **32**, 85–98 (2015).

32. Zhu, Z. G. et al. Adsorption-intensified degradation of organic pollutants over bifunctional α-Fe@carbon nanofibres. *Environ. Sci. Nano.* **4**, 302–306 (2017).

33. Yang, Y., Zhang, H. P. & Yan, Y. Synthesis of CNTs on stainless steel microfibrous composite by CVD: Effect of synthesis condition on carbon nanotube growth and structure. *Compos. Pt. B-Eng.* **160**, 369–383 (2019).

34. Yang, Y., Zhang, H. P. & Yan, Y. The preparation of Fe2O3-ZSM-5 catalysts by metal-organic chemical vapour deposition method for catalytic wet peroxide oxidation of m-cresol. *R. Soc. Open Sci.* **5**, 171731 (2018).

35. Yang, Y. et al. Lanthanum carbonate grafted ZSM-5 for superior phosphate uptake: Investigation of the growth and adsorption mechanism. *Chem. Eng. J.* **430**, 133166 (2022).

36. Yang, Y. et al. Construction of a novel lanthanum carbonate-grafted ZSM-5 zeolite for effective highly selective phosphate removal from wastewater. *Microporous Mesoporous Mat.* **324**, 111289 (2021).

37. Sing, K. S. W. Reporting physisorption data for gas/solid systems with special reference to the determination of surface area and porosity (Recommendations 1984). *Pure Appl. Chem.* **54**, 2201–2218 (1982).

38. Chen, W. R. et al. Efficient adsorption of Norfloxacin by Fe-MCM-41 molecular sieves: Kinetic, isotherm and thermodynamic studies. *Chem. Eng. J.* **281**, 397–403 (2015).

39. Xu, N. K., Guo, D. Y. & Xiao, C. F. Fe/Mn oxide decorated polyacrylonitrile hollow fiber membrane as heterogeneous Fenton reactor for methylene blue decolorization. *J. Appl. Polym. Sci.* **136**, 48217 (2019).

40. Wang, J. W. et al. Gravity-driven catalytic nanofibrous membrane with microsphere and nanofiber coordinated structure for ultrafast continuous reduction of 4-nitrophenol. *J. Colloid Interface Sci.* **538**, 108–115 (2019).

41. Khataee, A. R., Zarei, M. & Moradkhannejhad, L. Application of response surface methodology for optimization of azo dye removal by oxalate catalyzed photoelectro-Fenton process using carbon nanotube-PTFE cathode. *Desalination* **258**, 112–119 (2010).

42. Watson, M. et al. Response surface methodology investigation into the interactions between arsenic and humic acid in water during the coagulation process. *J. Hazard. Mater.* **312**, 150–158 (2016).

43. Danmaliki, G. I., Saleh, T. A. & Shamsuddeen, A. A. Response surface methodology optimization of adsorptive desulfurization on nickel/activated carbon. *Chem. Eng. J.* **313**, 993–1003 (2017).

44. Moura, F. C. et al. Efficient use of Fe metal as an electron transfer agent in a heterogeneous Fenton system based on Fe0/Fe3O4 composites. *Chemosphere* **60**, 1118–1123 (2005).

45. Yang, Y. et al. An innovative lanthanum carbonate grafted microfibrous composite for phosphate adsorption in wastewater. *J. Hazard. Mater.* **392**, 121952 (2020).

46. Mahmoudi, K., Hosni, K., Hamdi, N. & Srasra, E. Kinetics and equilibrium studies on removal of methylene blue and methyl orange by adsorption onto activated carbon prepared from date pits-A comparative study. *Korean J. Chem. Eng.* **32**, 274–283 (2015).

47. Azeroual, S., Wattati, H., Belfkira, A., Taourirte, M. & Jalal, R. Preparation and application of phosphorylated starch as a flocculant for cationic dyes and heavy metal. *Colloids Surf. C: Environ. Asp.* **1**, 100019 (2023).

48. Rusevova, K. et al. LaFeO3 and BiFeO3 perovskites as nanocatalysts for contaminant degradation in heterogeneous Fenton-like reactions. *Chem. Eng. J.* **239**, 322–331 (2014).

49. Bautista, P., Mohedano, A. F., Menéndez, N., Casas, J. A. & Rodriguez, J. J. Catalytic wet peroxide oxidation of cosmetic wastewaters with Fe-bearing catalysts. *Catal. Today* **151**, 148–152 (2010).

50. Yi, S. X. et al. Scalable fabrication of bimetal modified polyacrylonitrile (PAN) nanofibrous membranes for photocatalytic degradation of dyes. *J. Colloid Interface Sci.* **559**, 134–142 (2020).

51. Masomboon, N., Ratanatamskul, C. & Lu, M. Chemical oxidation of 2,6-dimethylaniline in the fenton process. *Environ. Sci. Technol.* **43**, 8629–8634 (2009).

52. Park, J., Wang, J. J., Park, K. H. & Seo, D. Heterogeneous fenton oxidation of methylene blue with Fe-impregnated biochar catalyst. *Biochar* **2**, 165–176 (2020).

53. Han, Z. B., Li, J. F., Han, X., Ji, X. J. & Zhao, X. M. A comparative study of iron-based PAN fibrous catalysts for peroxymonosulfate activation in decomposing organic contaminants. *Chem. Eng. J.* **358**, 176–187 (2019).

54. Yang, Y., Zhang, H. P., Huang, H. X., Yan, Y. & Zhang, X. Y. Iron-loaded carbon nanotube-microfibrous composite for catalytic wet peroxide oxidation of m-cresol in a fixed bed reactor. *Environ. Sci. Pollut. Res*. **27**, 6338–6351 (2020).

55. Liu, P. J., He, S. B., Wei, H. Z., Wang, J. H. & Sun, C. L. Characterization of α-Fe2O3/γ-Al2O3 Catalysts for Catalytic Wet Peroxide Oxidation of m-Cresol. *Ind. Eng. Chem. Res.* **54**, 130–136 (2015).

56. Liu, X. J. et al. Construction of Z-scheme CuFe2O4/MnO2 photocatalyst and activating peroxymonosulfate for phenol degradation: Synergistic effect, degradation pathways, and mechanism. *Environ. Res.* **200**, 111736 (2021).

57. Yang, B., Tian, Z., Zhang, L., Guo, Y. P. & Yan, S. Q. Enhanced heterogeneous Fenton degradation of Methylene Blue by nanoscale zero valent iron (nZVI) assembled on magnetic Fe3O4/reduced graphene oxide. *J. Water Process. Eng.* **5**, 101–111 (2015).

58. Rache, M. L. et al. Azo-dye orange II degradation by the heterogeneous Fenton-like process using a zeolite Y-Fe catalyst—Kinetics with a model based on the Fermi's equation. *Appl. Catal. B-Environ.* **146**, 192–200 (2014).

59. Yang, B. et al. Simultaneous removal of methylene blue and total dissolved copper in zero-valent iron/H2O2 Fenton system: Kinetics, mechanism and degradation pathway. *J. Colloid Interface Sci.* **555**, 383–393 (2019).

60. Yi, Q. Y. et al. Singlet oxygen triggered by superoxide radicals in a molybdenum cocatalytic Fenton reaction with enhanced REDOX activity in the environment. *Environ. Sci. Technol.* **53**, 9725–9733 (2019).

61. Chen, M. Q., Chen, Z. H., Wu, P. X. & Chen, J. P. Simultaneous oxidation and removal of arsenite by Fe (III)/CaO2 Fenton-like technology. *Water Res.* **201**, 117312 (2021).
62. Shan, S. J. et al. Decontamination of arsenite by a nano-sized lanthanum peroxide composite through a simultaneous treatment process combined with spontaneously catalytic oxidation and adsorption reactions. *Chem. Eng. J.* **435**, 135082 (2022).
63. Santos-Juanes, L., García-Ballesteros, S., Vercher, R. F., Amat, A. M. & Arques, A. Commercial steel wool used for Zero Valent Iron and as a source of dissolved iron in a combined red-ox process for pentachlorophenol degradation in tap water. *Catal. Today* **328**, 252–258 (2019).
64. Yang, Y., Zhang, H. P., Huang, H. X., Yan, Y. & Zhang, X. Y. Degradation of m-cresol over iron loaded carbon nanotube microfibrous composite: Kinetic optimization and deactivation study. *Sep. Purif. Technol.* **262**, 118340 (2021).
65. Hosseini, M. et al. Promotional effect of gold added to palladium supported on a new mesoporous TiO2 for total oxidation of volatile organic compounds. *Catal. Today* **122**, 391–396 (2007).
66. Zha, S. X. et al. Nanoscale zero-valent iron as a catalyst for heterogeneous Fenton oxidation of amoxicillin. *Chem. Eng. J.* **255**, 141–148 (2014).
67. Yue, Z. R., Jiang, W., Wang, L. C., Gardner, S. D. & Pittman, C. U. Surface characterization of electrochemically oxidized carbon fibers. *Carbon* **37**, 1785–1796 (1999).
68. Liu, C. X., Li, X., Ma, B., Qin, A. W. & He, C. J. Removal of water contaminants by nanoscale zero-valent iron immobilized in PAN-based oxidized membrane. *Appl. Surf. Sci.* **321**, 158–165 (2014).
69. Yang, Y., Zhang, H. P. & Yan, Y. Synthesis of carbon nanotube on stainless steel microfibrous composite—Comparison of direct and indirect growth and its application in fixed bed m-cresol adsorption. *Chem. Eng. Res. Des.* **139**, 162–173 (2018).
70. Datsyuk, V. et al. Chemical oxidation of multiwalled carbon nanotubes. *Carbon* **46**, 833–840 (2008).
71. Dong, Y. C., Han, Z. B., Liu, C. Y. & Du, F. Preparation and photocatalytic performance of Fe (III)-amidoximated PAN fiber complex for oxidative degradation of azo dye under visible light irradiation. *Sci. Total Environ.* **408**, 2245–2253 (2010).

Acknowledgements

Author contributions

Yang: concept formation, technical writing, funding; Lin: material development, experimental study; Long: experimental study; Mei: experimental study; Chen: technical writing, revision, supervision.

Competing interests

The authors declare no competing interests.

Additional information

Supplementary information The online version contains supplementary material available at https://doi.org/10.1038/s41545-024-00333-6.

Correspondence and requests for materials should be addressed to Yi Yang or J. Paul Chen.

Reprints and permissions information is available at http://www.nature.com/reprints

Publisher's note Springer Nature remains neutral with regard to jurisdictional claims in published maps and institutional affiliations.